Meteorological, snow and soil data, CO_2, water and energy fluxes, from a low-Arctic valley of Northern Quebec

Florent Domine[1,2,3], Denis Sarrazin[2], Daniel F. Nadeau[4,5], Georg Lackner[1,2,4,6], and Maria Belke-Brea[1,2,7]

[1]Takuvik Joint International Laboratory, Université Laval (Canada) and CNRS-INSU (France), Québec, Canada
[2]Centre d'Études Nordiques, Université Laval, Québec, Canada
[3]Department of Chemistry, Université Laval, Québec, Canada
[4]Department of Civil and Water Engineering, Université Laval, Québec, Canada
[5]CentrEau, Université Laval, Québec, Canada
[6]CNRM, Université de Toulouse, Météo-France, CNRS, Toulouse, France
[7]Presently at: Department of Biology, Wilfrid Laurier University, Waterloo, Canada

Correspondence to: Florent Domine (florent.domine@gmail.com)

Abstract. As the vegetation in the Arctic changes, tundra ecosystems along the southern border of the Arctic are becoming greener and gradually giving way to boreal ecosystems. This change is affecting local populations, wildlife, energy exchange processes between environmental compartments, and the carbon cycle. To understand the progression and the implications of this change in vegetation, satellite measurements and surface models can be employed. However, in situ observational data are required to validate these measurements and models. This paper presents observational data from two nearby sites in the forest–tundra ecotone in the Tasiapik Valley near Umiujaq in Northern Quebec, Canada. One site is on a mixture of lichen and shrub tundra. The associated data set comprises 9 years of meteorological, soil and snow data as well as 3 years of eddy covariance data. The other site, 850 m away, features vegetation consisting mostly of tall shrubs and black spruce. For that location, 6 years of meteorological, soil and snow data are available. In addition to the data from the automated stations, profiles for snow density and specific surface area were collected during field campaigns. The data are available at https://doi.org/10.1594/PANGAEA.XXXXXX (Domine et al., 2024).

1 Introduction

The forest–tundra ecotone (FTE) marks a transition zone where the open-canopy forest of the boreal biome merges with the treeless Arctic tundra biome. According to Callaghan et al. (2002), the FTE spans more than 13 400 km across the northern parts of North America, Asia, and Europe, with a width of up to several hundred kilometers. This makes it the world's largest vegetation transition zone. A trend towards increased vegetation has been observed in the FTE. In fact, the above-ground biomass is on the rise for all Arctic environments (Meredith et al., 2019). Future projections indicate that the areal extent of tundra vegetation will decrease by at least 50% by 2050 (Pearson et al., 2013), while woody shrubs and trees will expand to 24–52% of the current tundra region, or 12–33% if tree dispersal is restricted (Meredith et al., 2019). This change will have major repercussions, such as large reductions in the soil carbon content due to more frequent wildfires (Mack et al., 2011) and widespread permafrost degradation occurring at increased rates compared to when only the changing environmental conditions are considered (Jones, 2015).

To understand, quantify, and project changes in the FTE, satellite monitoring and surface modeling are essential. However, both require in situ measurements. Although satellites cover large parts of the Earth's surface and are able to estimate a variety of surface-related variables (e.g., surface temperature (Qu et al., 2019), turbulent heat fluxes (Jiménez et al., 2017), vegetation cover (Guo et al., 2020)), most must be calibrated and/or validated using point measurements (e.g., Boisvert et al. (2015); Riihelä et al. (2017); Martin et al. (2019)). Surface schemes for climate models also require validation using in situ data (Krinner et al., 2018). Despite this need for data, few stations in Arctic regions are equipped to measure large sets of variables over long periods of time.

The Tasiapik Valley in northern Quebec, Canada is located within the FTE (Latifovic et al., 2017). This is an ideal location for conducting research because the lower valley is covered in open boreal forest while the upper valley consists of shrub and lichen tundra. Arctic and boreal biomes, as well as mixtures of both, are therefore present in close proximity to each other. Meteorological, snow, and soil data were collected starting in September 2012, and annual field surveys were conducted to study snow and soil characteristics (Domine et al., 2015). Turbulent heat fluxes were measured between 2017 and 2020 using the eddy covariance technique.

Detailed annual snowpit data are extremely valuable, as studies have shown that current snow models struggle to accurately simulate vertical profiles of density and thermal conductivity (Domine et al., 2016; Barrere et al., 2017; Gouttevin et al., 2018; Royer et al., 2021; Lackner et al., 2022a). Although new models are being developed to account for this deficiency (Jafari et al., 2020; Simson et al., 2021), critical validation data for snow density profiles remain very rare in the Arctic. In this paper, we present information on two research sites while fully documenting all the available data and providing a detailed analysis of the soil properties at the sites. We provide a comprehensive data set with meteorological, snow, soil, and turbulent flux data from 2012 to 2021.

2 Site Description

The study site is located in the Tasiapik Valley (Fig. 1) close to the village of Umiujaq, Quebec, Canada (56.55861°N, 76.48222°W). The valley forms a small catchment 4.5 km long and 1.3 km wide, and borders Tasiujaq Lake at an elevation of 0 m. The climate is subarctic with a mean annual temperature of −4.0°C. No long-term precipitation records exist, but our recent data indicate a rather high mean annual precipitation compared to typical subarctic climates, at between 800 and 1000 mm. Around 50% of the precipitation occurs as snow. There is usually continuous snow cover from late October to early June. Hudson Bay to the west of the valley (4 km distance) strongly influences the weather pattern. There is frequent fog throughout the year (Robichaud and Mullock, 2001). Advection fog often forms in July and August when warmer air moves over the cold Hudson Bay. The precipitation pattern is influenced by the extent of the ice cover in Hudson Bay. After freeze-up, the precipitation rate drops and remains rather low until spring. Precipitation then increases in summer and peaks in late summer and fall. The heat storage of Hudson Bay in summer and the subsequent release in fall also affects air temperatures, resulting in relatively cold summer temperatures and warmer fall temperatures.

In Tasiapik Valley, vegetation is fairly spatially heterogeneous. In the upper valley, a mixture of lichen (*Cladonia* sp., mostly *C. stellaris* and *C. rangiferina*), and shrubs with dwarf birch (*Betula glandulosa*), and other shrub species (*Vaccinium* sp., *Alnus viridis* subsp. *crispa* and *Salix* sp. including *S. planifolia*) with heights between 0.2 and 2 m dominate. Live lichens are present not only on lichen tundra, but also in the understory of birches less than 80 cm tall. Live lichen can form layers 5 to 20 cm thick over a 2 to 4 cm layer of dead lichen, progressively transitioning to a thin organic litter layer (Gagnon et al., 2019). The litter layer is only about 2 cm thick under lichen tundra and up to 5 cm thick under 80 cm tall birch. Taller birches such as those found in water tracks have a mossy understory with a 10 cm thick organic layer (Gagnon et al., 2019). Towards the bottom of the valley, vegetation turns into a forest-tundra with black spruce (*Picea mariana*) covering about 20% of the surface. Below the open canopy, numerous birches are present. In areas not covered by woody vegetation, a variety of grasses and mosses cover the surface.

There is discontinuous to sporadic permafrost in the valley (Lemieux et al., 2020) as witnessed by the presence of permafrost mounds (lithalsas). At the exact location of the experimental setup, no permafrost was present. However, lithalsas were found within 30 m of the upper valley site. The soil composition is detailed in Sect. 7.

On 28 September 2012, a comprehensive meteorological station called TUNDRA (56.55877°N, 76.48234°W; elevation: 132 m) was deployed (Figure 1). Instruments were placed on a tripod. On 15 February 2013, snow temperature and thermal conductivity sensors were installed on a vertical post a few m from the tripod, in dwarf birch 30 cm tall (Domine et al., 2015). The heights and number of instruments were modified on 19 September 2015, while soil temperature and humidity sensors were installed. One set of soil instruments was located under lichen, and one under low birch near the post holding the snow sensors.

The FOREST station (56.55308°N, 76.47258°W, elevation: 82 m) was set up on 21 September 2015 with the same instruments as those at the TUNDRA station. A fast-response gas analyzer with a sonic anemometer (model IRGASON, Campbell

Scientific, USA) was mounted at a 10 m tower about 15 m north of the TUNDRA station on 10 June 2017 and was operational until 30 April 2020. A second post with temperature and thermal conductivity sensors was installed on 20 September 2018 on lichen with no shrubs, about 15 m northwest of the tripod at TUNDRA. Multiple Reconyx time lapse cameras took several pictures per day and were installed in order to monitor the instrumentation and their surroundings. A complete list of all instruments deployed at TUNDRA and FOREST, as well as when each instrument was installed and at what precise position, is provided in Tables 1 and 2, respectively. The data obtained are available in Lackner et al. (2022b). All times are UTC.
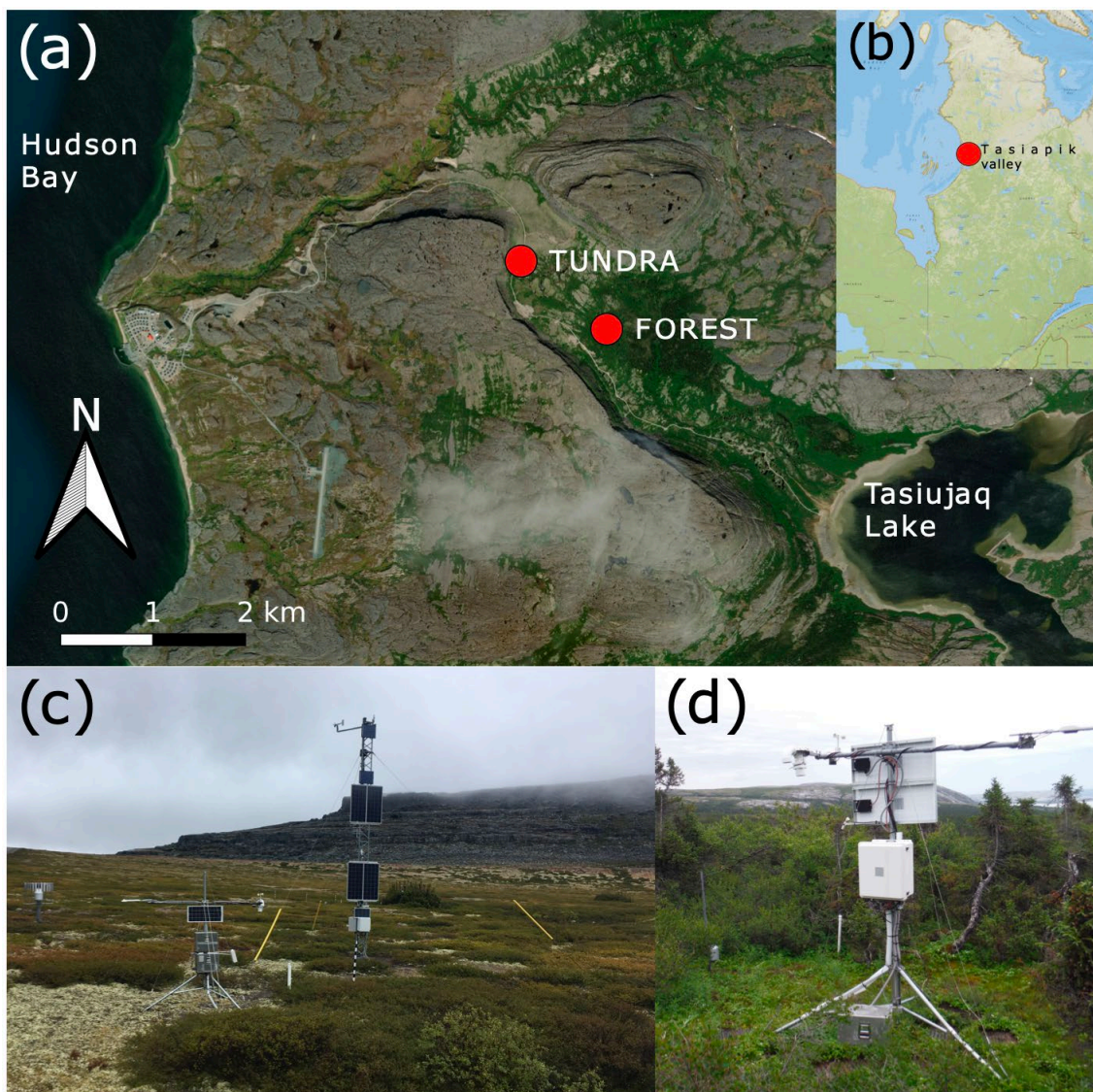
Figure 1: (a) Location of the two sites in the Tasiapik Valley. (b) Location of the valley along the eastern shore of Hudson Bay in Northern Quebec. (c) Photo of the instrumentation at TUNDRA. Most instruments are on the tripod. The precipitation gauge is visible on the left. The IRGASON and instruments used for data gap-filling are on the 10-m tower. (d) The instrumentation at FOREST. Source (a and b): ESRI.

3 Climate Data

3.1 Air Temperature, Humidity, Atmospheric Pressure, and Wind Speed

3.1.1 TUNDRA

Air temperature and relative humidity (RH) were measured at TUNDRA with a HC2-S3-XT sensor installed at a height of 2.3

105 m. No large data gaps were present. Small data gaps were filled using information from a similar sensor mounted close by on the 10-m tower (see Fig. 1c). As the RH measurements never reached ice saturation in winter, we corrected the raw values using linear equations based on air temperature in order to reach ice saturation. The method has been detailed in Domine et al. (2021).

Table 1: Instrumentation at the TUNDRA study site.

Variable	Instrument	Manufacturer	Height/Depth	Years available	Comment
Air temperature and humidity	HC2-S3-XT sensor, inside white PVC tubing, ventilated	Rotronic	2.3 m	2012–2021	
Atmospheric pressure	IRGASON	Campbell Scientific	4.2 m	2017–2020	Before 2017 and after 2020 corrected ERA5 data
Wind speed	A100 Cup anemometer	Vector instruments	2.3 m	2012–2021	
Radiation	CNR4 with CNF4 heater/ventilator	Kipp & Zonen	2.3 m	2012–2021	
Precipitation	T-200 BM	Geonor	2.3 m	2016–2021	Data before 2016 from uncorrected ERA5
Snow depth	SR50 acoustic gauge	Campbell Scientific		2012–2021	
Snow temperature	Pt1000 thermistor	Hukseflux	4, 14, 34, 44 cm	2/2013-5/2015	Near TUNDRA (SNOW1)
Snow temperature	Pt1000 thermistor	Hukseflux	4, 14, 29, 44 and 64 cm	10/2015–2021	Near TUNDRA (SNOW1)
Snow thermal conductivity	TP08	Hukseflux	4, 14, 34, 44 cm	2/2013-5/2015	Near TUNDRA (SNOW1)
Snow thermal	TP08	Hukseflux	4, 14, 29, 44 and 64	10/2015–2021	Near TUNDRA

			cm		(SNOW1)
Snow thermal conductivity	TP08	Hukseflux	7, 27, 47, 67 cm	2018–2020	Near TUNDRA (SNOW2)
Soil temperature and volumetric water content	Decagon 5TM	Decagon (now METER)	−6, −12, −21, −32, −50 cm	2015–2021	Near TUNDRA under lichen
Soil temperature and volumetric water content	Decagon 5TM	Decagon (now METER)	−9, −15, −27, −39, −50 cm	2015–2021	Near TUNDRA under shrubs
Scenery	Time lapse camera	Reconyx	1.5 m	2015–2021	Multiple cameras pointing different directions

110

Table 2: Instrumentation at the FOREST study site.

Variable	Instrument	Manufacturer	Height/Depth	Years available	Comment
Air temperature and humidity	HC2-S3-XT sensor, inside white PVC tubing, ventilated	Rotronic	2.3 m	2015–2021	
Wind speed	Cup anemometer	Vector instruments	2.3 m	2015–2021	
Radiation	CNR4 with CNF4 heater/ventilator	Kipp & Zonen	2.3 m	2015–2021	
Snow depth	SR50 acoustic gauge	Campbell Scientific		2015–2021	
Snow temperature	Pt1000	Hukseflux	4, 14, 29, 64 cm	2015–2021	Near FOREST (SNOW3)
Snow thermal conductivity	TP08	Hukseflux	4, 14, 29, 64 cm	2015–2021	Near FOREST (SNOW3)
Soil temperature and volumetric water content	Decagon 5TM	Decagon (now METER)	−5, −10, −20, −30, −50 cm	2015–2021	Near FOREST

From June 2017, measurements of specific humidity (SH) were collected with an IRGASON infrared gas analyzer. However, this instrument is susceptible to measurement errors caused by rain, snow, dew, or any other particle within the pathway of the gas analyzer. Complications with the IRGASON analyzer are detailed in Section 5. Gaps in the SH time series were filled using converted RH measurements. The atmospheric pressure for SH was measured from June 2017 onward with the IRGASON

analyzer. Before that date and after dismantling the instrument in April 2020, ERA5 data were used. ERA5 is a reanalysis product (Hersbach et al., 2020) from the European Centre for Medium-Range Weather Forecast that provides hourly estimates for various meteorological and soil variables starting from 1959, at a spatial resolution of 30 km (https://www.ecmwf.int/en/forecasts/datasets/reanalysis-datasets/era5). However, as the ERA5 data do not correspond with the same elevation, we corrected for a ≈10 hPa offset between the ERA5 data and the observations that was detected for times when both sets of data were available. Except for two long power outages (see Section 5), there were no other significant gaps in the time series for pressure. The gaps from the power outages were filled using the corrected ERA5 data.

Wind speed data were collected with a cup anemometer at a height of 2.3 m at TUNDRA. In winter, the instrument was sometimes stalled due to frost during stable, low-wind conditions. To fill those gaps, we used data from a Young anemometer affixed at a height of 10 m on the nearby tower (CEN,1997–2020), visible in Fig. 1c. At times, the Young anemometer became covered in ice at the same time as the cup anemometer. During those times, we used the data from the FOREST station, where the instrument was installed at the same height as at TUNDRA. During one period in January 2021, all available instruments in the valley were stalled. We therefore used an instrument from the UMIROCA station (CEN, 1997-2020), a station located on the shore of Hudson Bay. All data used to fill the gaps were corrected using a linear regression. This was done to account for different installation heights and environments (vegetation, elevations, topography). Figure 2 shows the time series of the variables mentioned above.
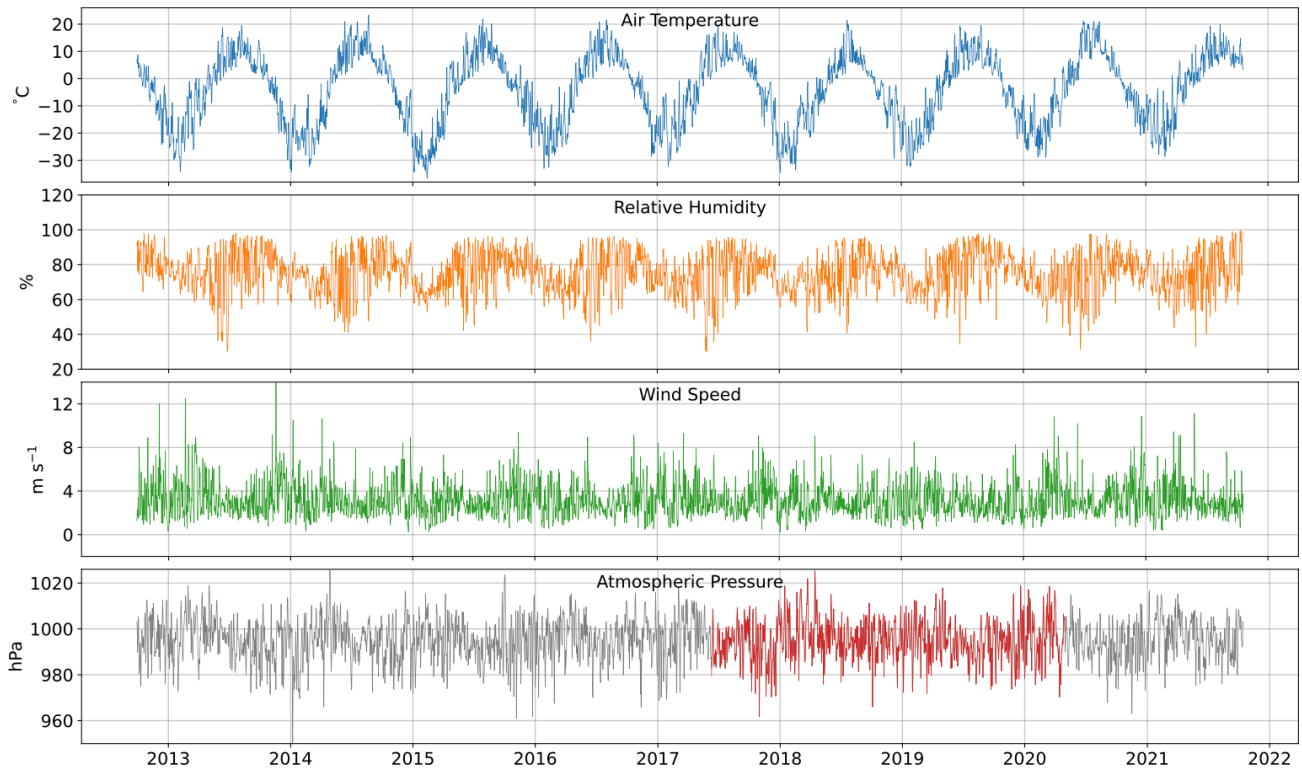
Figure 2: Time series of hourly air temperature, relative humidity, wind speed, and atmospheric pressure at TUNDRA. The red section of the atmospheric pressure curve represents local observations, while the grey sections represent corrected ERA5 reanalysis data.

3.1.2 FOREST

At the FOREST site, air temperature and wind speed were recorded with the same instruments as at TUNDRA (see Fig. 3). The temperature time series had no large gaps (> 3 h), and small gaps (≤ 3 h) were filled by interpolation. We used values from TUNDRA to gap-fill data for FOREST when the cup anemometer was ice-covered in winter, and applied a linear regression to adjust wind speeds. There was also an RH sensor at FOREST, but due to malfunctions, the recorded data could not be used.

Compared to TUNDRA, temperatures at FOREST were slightly higher throughout the year, except in November and December. From January 2016 to December 2020, the mean difference was ≈1°C. Since the surface roughness is greater at FOREST than at TUNDRA, wind speeds were lower for specific heights. Indeed, the mean wind speed from January 2016 to December 2020 was about ≈1 m s^{-1} lower at FOREST than at TUNDRA.
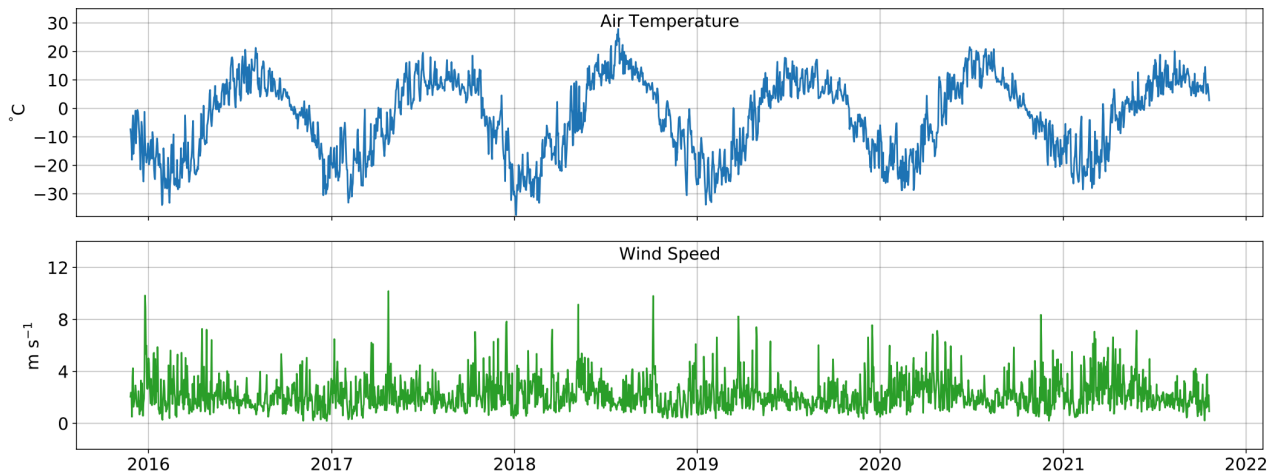
Figure 3: Time series of hourly air temperature and wind speed at FOREST.

3.2 Radiation

3.2.1 TUNDRA

The surface radiation terms were measured using a 4-component radiometer (model CNR4, Kipp & Zonen, The Netherlands) mounted at 2.3 m above ground. It was equipped with a CNF4 heating/ventilation unit (Kipp & Zonen, The Netherlands), which mostly prevented snow accumulation and the build-up of frost and dew on the measuring lenses. Frost was however

occasionally observed to partially cover the lenses during winter field trips. The CNF4 was programmed to be active for 5 min every hour, just before radiation measurements were collected.

From 10 October 2018 to 27 September 2020, no temperatures were recorded in the CNR4, which were otherwise used to correct the longwave radiation. During this period, we estimated CNR4 temperatures using a gradient boosting regressor from scikit-learn (Pedregosa et al., 2011) with the following input variables: air temperature, radiation, humidity, and wind speed. We trained the decision tree using data from periods when the CNR4 temperatures were recorded and found a good agreement between the observed and estimated values. Using the estimated temperatures, we calculated the longwave radiation (LW) using:

$$LW = (5.67 \times 10^{-8}) \frac{V}{C} T^4, \tag{1}$$

where V is the measured output voltage, C is the calibration constant and T is the temperature of the instrument in K.

In October 2018, the entire CNR4 unit was replaced and recalibrated. As the calibration constants had changed since installation, we applied a correction to account for the drift. We assumed that the calibration constants varied linearly over time between both calibrations. Between October 2018 and September 2021, no recalibration took place. We therefore used the constants of the instrument deployed in October 2018 without time variations.

Small, mostly negative values were observed at night for up- and downwelling shortwave radiation, although both these values are typically expected to be zero. To compensate for this discrepancy, we calculated the mean offset for both components and subtracted them from the respective upwelling and downwelling radiation.

Despite the CNF4 heating unit, the accumulation of frost and snow sometimes interfered with the incident radiation measurements (long and shortwave). The exact periods when the CNR4 sensors were impacted by frost and snow could only be determined visually. Since a detailed visual inspection could only be performed at the site, we applied several quality control criteria to the downwelling radiation (both long and shortwave) to exclude the affected periods. Therefore, all values at times when the wind speed was < 0.5 m s^{-1} or the uncorrected longwave downwelling radiation was > −5 W m^{-2} were discarded if the air temperature was < 0°C. Subsequently, gaps of up to 3 hours were interpolated, while longer gaps were filled using corrected ERA5 data. The correlation between ERA5 data and observations was established using the remaining data that passed our quality control measures. The 9-year time series for the 4 radiation components at TUNDRA are shown in Fig. 4.
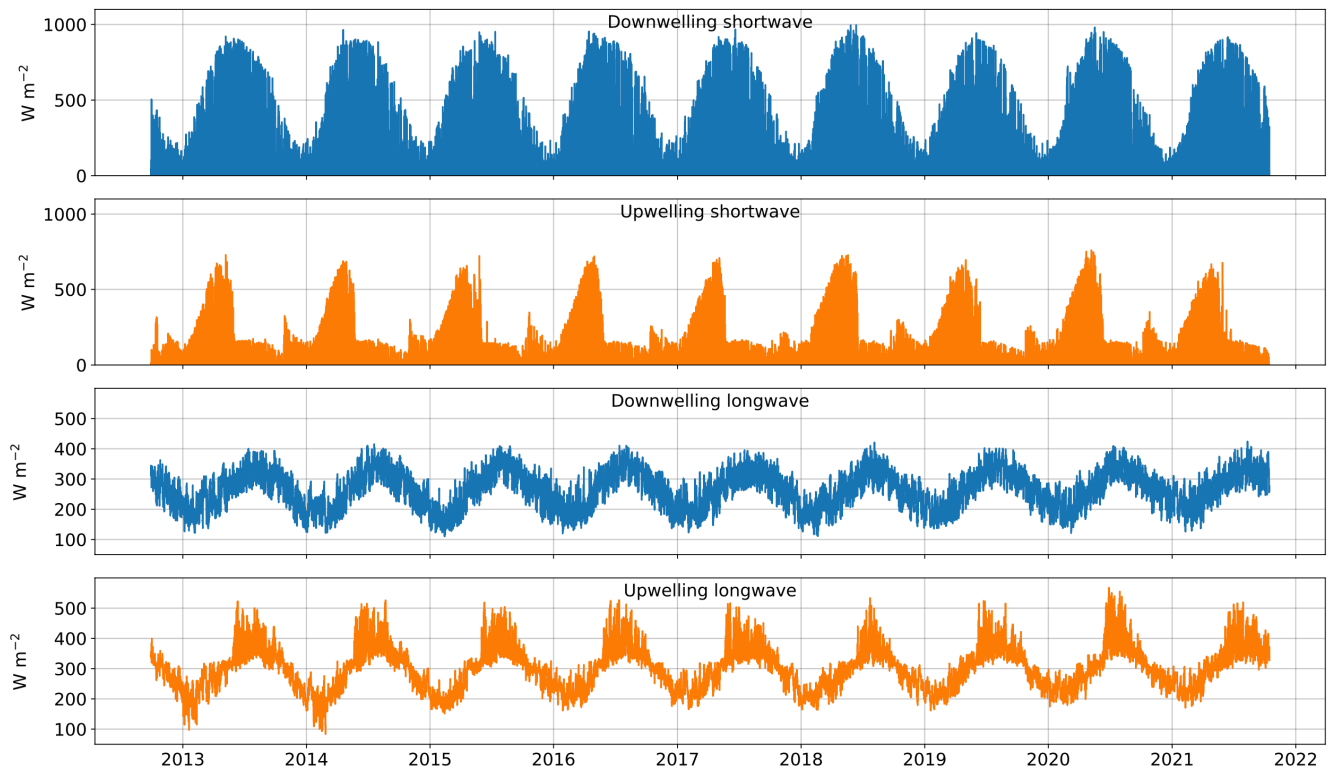
Figure 4: Time series of hourly downwelling and upwelling shortwave and longwave radiation at TUNDRA.

3.2.2 FOREST

The FOREST station setup was similar to that at TUNDRA, with a CNR4 radiometer at a height of 2.3 m combined with a CNF4 heating/ventilation unit. The CNR4 at FOREST was recalibrated in October 2021. The raw values were corrected for the drift of the calibration constants. No power outages or instrumental failures occurred at this site and the complete time series from 28 September 2015 is shown in Fig. 5. Frost buildup on the sensors was detected at described for the TUNDRA CNR4. Affected values were replaced with corrected ERA5 values.
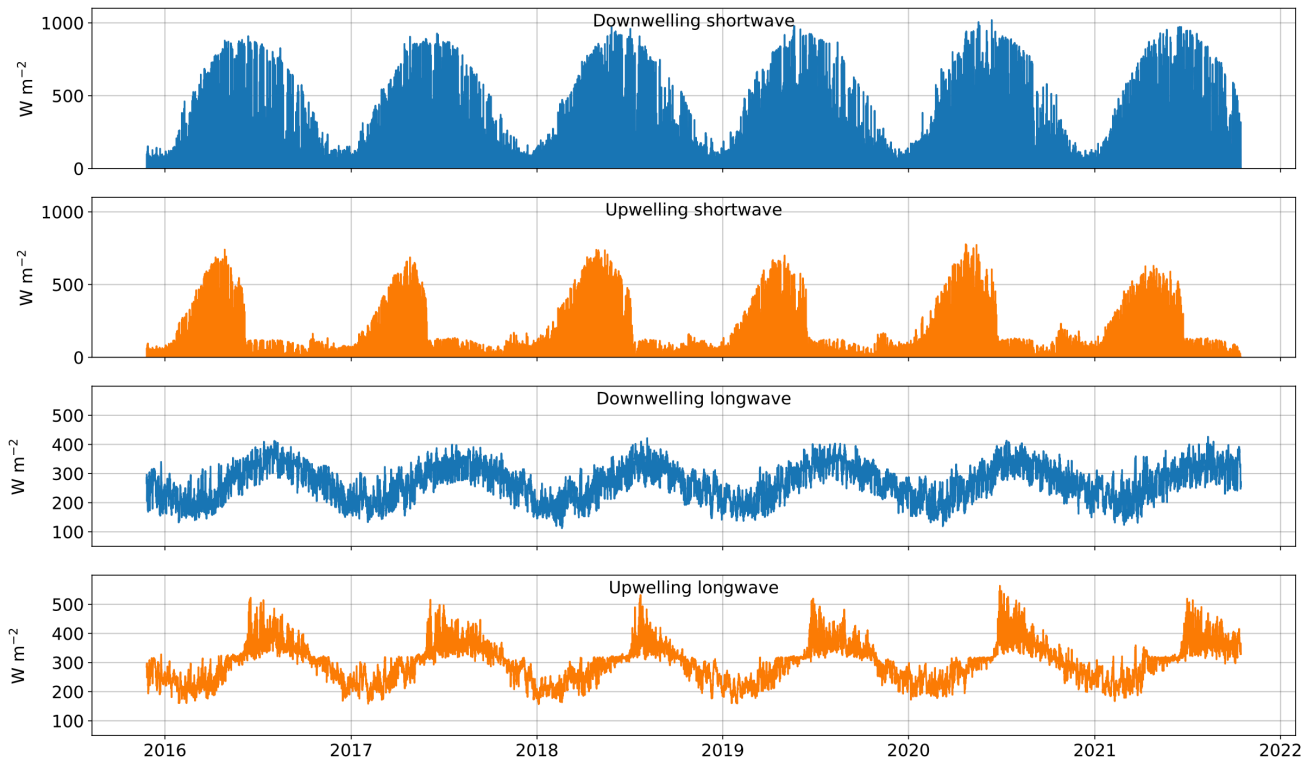
Figure 5: Time series of hourly downwelling and upwelling shortwave and longwave radiation at FOREST.

At FOREST, we also observed small, non-zero values at night for the shortwave radiation. To account for these offsets, we applied the same procedure as for TUNDRA. The same problems with frost and snow build-up were observed at FOREST. We applied the same criteria as for TUNDRA. The linear equations for the ERA5 data are also shown in the Supplementary Material.

Small differences became apparent when we compared the radiation observations at both sites. The downwelling shortwave radiation was smaller at FOREST, which can be attributed to greater topographic shading by the cuestas, as FOREST is a lower elevation than TUNDRA. Between January 2016 and December 2020, the mean difference was 4.15 W m^{-2}. For the longwave radiation, there was very little difference in summer, but a small deviation was detected in winter when the longwave downwelling radiation was slightly higher at FOREST. This might be an effect of the higher vegetation levels at FOREST. Radiation from the steep cliffs surrounding the valley may also contribute to the longwave downwelling radiation. However, for the same 4-year period, the difference was only 1.5 W m^{-2}. Differences in upwelling radiation were slightly higher (TUNDRA−FOREST: 4.6 W m^{-2} for shortwave radiation and −2.15 W m^{-2} for longwave radiation). However, these values heavily depend on the radiative and thermal properties of the surface and soil, as well as on the duration of the snow-free period.

3.3 Precipitation

In May 2016, a T200B precipitation gauge (Geonor, USA) equipped with a single Alter shield was installed to measure solid and liquid precipitation close to the TUNDRA station. The gauge recorded hourly cumulative precipitation (PR_{tot}) in kg m^{-2} h^{-1}, equivalent to mm h^{-1}. The standard deviation (σ_i) of each hourly measurement was also recorded. The gauge has an inlet with a diameter of 16 cm and the rain/snow is collected in a cylinder with a capacity of 1000 mm. An anti-freeze agent was added in the cylinder to melt snow and keep the stored water from freezing. The use of an anti-freeze agent is preferable to a heating system, as heat increases water loss due to evaporation, particularly in summer. Evaporation is further reduced by adding a thin layer of oil to the water surface. Three vibrating wire load sensors weigh the entire cylinder and provide three independent measures for mass. First, the raw cumulative values from the three vibrating wire load sensors were transformed into hourly mass variations. Occasional erratic fluctuations occurred, induced by perturbations of the wire load sensors by the wind and other factors. Data that were obviously inconsistent given the latitude, for instance those beyond 30 mm h^{-1}, were eliminated and the three independent precipitation rates (PR_i with i = 1, 2, 3) were combined using a weighted mean. Each hour, the wire load sensor with the highest standard deviation (σ_i) was removed and the weighted mean was computed using the remaining two values, with the inverse of the standard deviation defining the weights as $w_i = 1/\sigma_i$, such that

$$PR_{tot} = \frac{w_1 PR_1 + w_2 PR_2}{w_1 + w_2}.$$

(2).

Subsequently, the precipitation was partitioned into snow and rain using a single threshold of 0.5°C. In addition, a correction for the underestimation of solid precipitation in the presence of wind (undercatch) was applied following Kochendorfer et al. (2018),

$$PR_{cor} = PR_{uncor} \frac{1}{0.742\exp(-0.181U+0.332)}$$

(3),

where PR_{cor} is the corrected precipitation rate in mm, PR_{uncor} is the uncorrected precipitation (in mm), and U (in m s^{-1}) is the wind speed at the height of the gauge orifice, provided by the nearby weather station. Prior to installing the precipitation gauge with the single alter shield and three independent wire load sensors, a simpler version with a home-made alter shield and only one wire load sensor was present at the site. However, this setup did not produce reasonable data and therefore the data were discarded. For the period between 2012 and 2016, we used only ERA5 data, as it proved to be closer to our observations than data from the two closest meteorological stations from Environment and Climate Change Canada (Kuujjuarapik, 160 km south and Inukjuak, 230 km north). When comparing summer and winter monthly precipitation observations with ERA5 data, we observed no biases for the summer values. However, we detected an underestimation of ERA5 for the winter months, with cumulative precipitation exceeding 50 mm. To correct for this bias, the values for November to April were multiplied by 1.3822 for months with a cumulative precipitation greater than 50 mm. Otherwise, no correction was applied to the ERA5 precipitation

data.

240   In the lower panel in Fig. 6, the daily precipitation at TUNDRA is shown from 2016 to 2021, as well as the ERA5 precipitation data before 2016. The upper panel in Fig. 6 depicts the seasonal cumulative precipitation for each summer and winter period, respectively. The dates associated with the onset of snow and meltout are shown in Table 3, and were determined using snow gauge data and time lapse cameras.
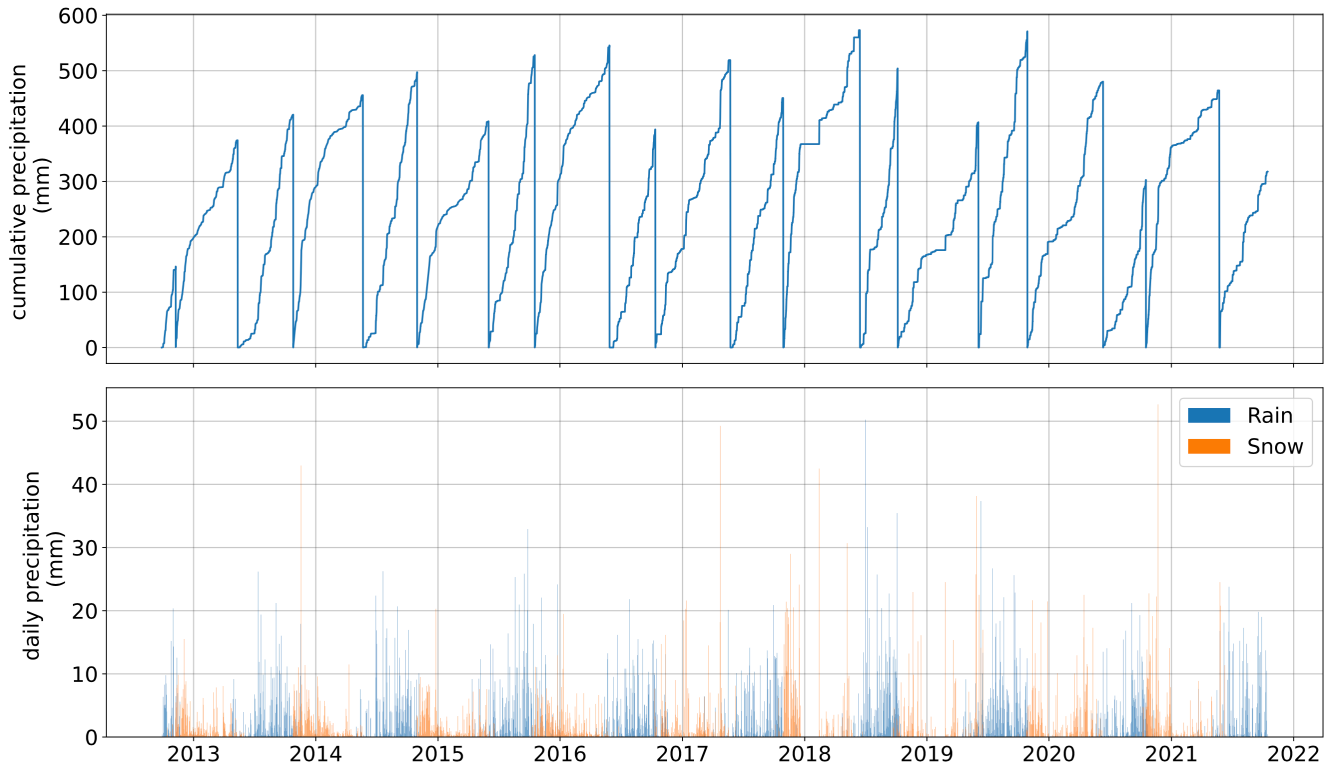
245   **Figure 6: Time series of cumulative precipitation and daily rain and snow. Before 28 May 2016, ERA5 data were used.**

250

Table 3: Snow onset and meltout dates at the TUNDRA site, used to determine cumulative seasonal precipitation.

Snow year	Snow onset	Meltout
2012–13	9 November 2012	31 May 2013
2013–14	26 October 2013	22 May 2014

2014–15	31 October 2014	28 May 2015
2015–16	18 October 2015	28 May 2016
2016–17	12 October 2016	24 May 2017
2017–18	29 October 2017	15 June 2018
2018–19	6 October 2018	4 June 2019
2019–20	29 October 2019	11 June 2020
2020–21	17 October 2020	24 May 2021

4. Spectral and Broadband Albedo

The surface albedo for various types of vegetation covers was measured between 12 and 18 September 2015 for wavelengths between 346.5 and 2513 nm with a portable field spectroradiometer (HR-1024 model, Spectra Vista Corporation). The radiation signal over this spectral range was monitored with a Si photodiode (346.5 to 982 nm) and two InGaAs photodiodes over the 982–1882 and 1882–2513 nm ranges. For wavelengths greater than 2340 nm, upwelling irradiance was very low, resulting in a mostly unusable signal. We therefore present only the results for the 346.5–2340 nm range. The radiation signal was collected by an integrating sphere placed at the end of a 3 m rod to minimize interference from the person taking the measurements. The horizontal position of the sphere was ensured by an electronic inclinometer next to the sphere. The downwelling signal was collected first. Then, the sphere was rotated 180° to record the upwelling signal. A photodiode monitored the solar radiation to ensure that it remained constant (within 1%) during both measurements. Spectra were smoothed over 10 nm intervals for wavelengths shorter than 1780 nm, and over 60 nm intervals for longer wavelengths.

Spectra were recorded during the 12 to 16 September 2015 period. Five spectra were recorded over areas with lichen cover in the vicinity of the TUNDRA site. Five spectra were also recorded over short birch shrubs with lichen understories in the same area. We visually estimated that > 90% of the leaves were still green. The FOREST site consisted of a mixture of spruce that reached up to 3 m high, birch and grass. As such, it was not possible to obtain a representative spectrum of the entire FOREST area, as this would have required measurements from a height of at least 10 m. We therefore measured eight spectra of dense, short spruce within a few km of the FOREST station (Fig. 7). Lastly, we measured the spectra of grassy surfaces with little to no erect vegetation and with little to no lichen. Although these spectra were not necessarily recorded at the FOREST site, the grassy vegetation was fairly similar at both locations. The average spectra for all four types of vegetation are shown in Fig. 7. The broadband (BB) albedo (346.5–2340 nm) of each spectrum was calculated from the ratio of the integrated upwelling radiation to downwelling radiation. The average BB albedos were 0.203 for lichen, 0.155 for birch, 0.174 for spruce and 0.180 for low grassy vegetation.
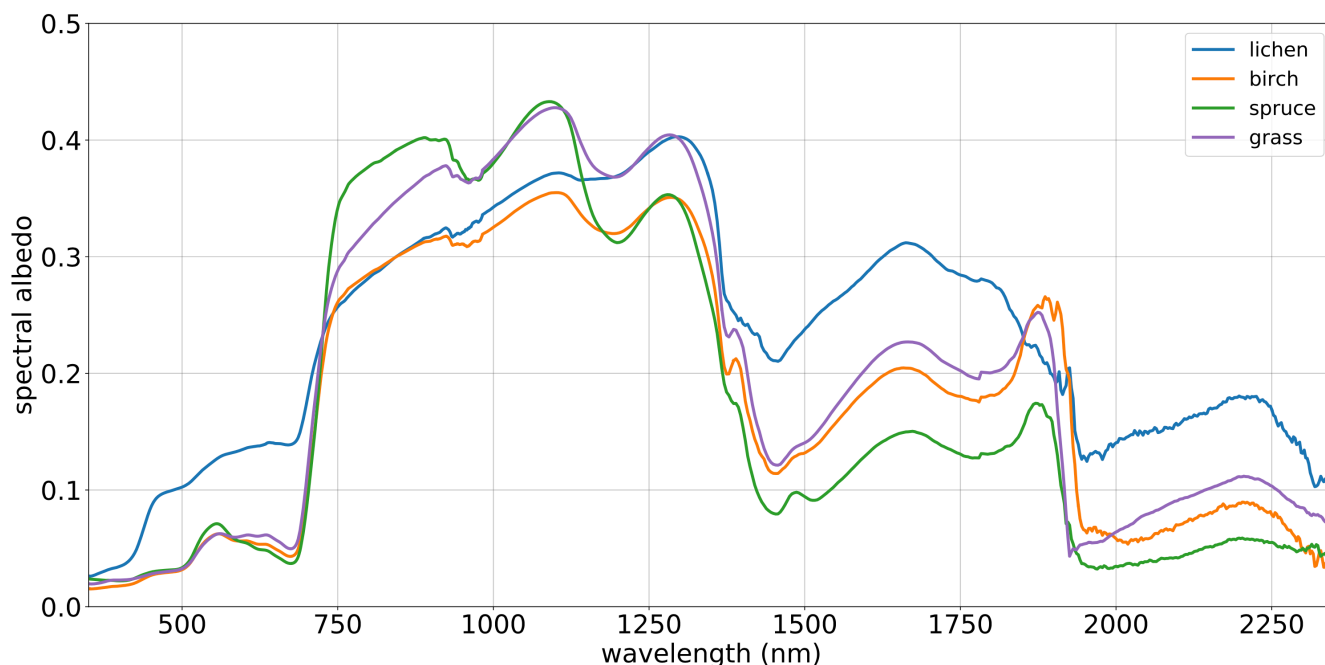
275

Figure 7: Average spectral albedo for the four types of vegetation cover.

For a given vegetation type, variations in the spectral albedo were observed among the different measurement spots, as detailed in Table 4. Variations between spots were smallest for lichen, increased for birch and low grassy vegetation, and were highest for spruce. Variations in birch and spruce are probably mostly due to differences in the leaf area index and in the amount of woody

280 vegetation present. Differences in low grassy vegetation are due to variations in species and the occasional presence of short shrubs, such as *Vaccinuim sp.* and *Betula glandulosa*.

Table 4: Variation in albedo within each vegetation class, at 550 and 1100 nm.

	550 nm	550 nm % variation	1100 nm	1100 nm % variation
Lichen	0.116 to 0.131	11.5%	0.359 to 0.393	8.6%
Low birch	0.051 to 0.067	23.9%	0.305 to 0.387	21.2%
Spruce	0.058 to 0.107	45.8%	0.355 to 0.559	36.5%
Low grassy	0.053 to 0.080	33.7%	0.370 to 0.523	29.3%

285 These data allowed for the estimation of the BB albedo of the FOREST site. We estimated that the vegetation coverage is 25% spruce, 40% low grassy vegetation, and 35% birch, leading to a BB albedo of 0.170. We estimated the TUNDRA site to be 60% lichen and 40% birch, with a BB albedo of 0.184.

5 Turbulent Flux Data

290   Turbulent heat fluxes were measured at TUNDRA using a fast-response sonic anemometer and a CO_2/H_2O infrared gas analyzer (IRGASON, Campbell Scientific, USA) installed 4.2 m above ground on the 10-m tower. The three components for wind speed and concentrations of H_2O and CO_2 were recorded with a CR3000 datalogger (Campbell Scientific) at a frequency of 10 Hz. The 10-Hz data were processed with the EddyPro® (version 7.0.3; Li-COR Biosciences, USA) software package. This software calculates 30-min averages of the turbulent heat and carbon fluxes and a set of corrections. These corrections are

295   the detrending of turbulent fluctuations based on a running mean, covariance maximization, density fluctuation compensation (Webb et al., 1980), and analytic correction of high-pass and low-pass filtering effects (Moncrieff et al., 1997). To align the coordinate system with the surface, we have chosen to apply a double rotation (Wilczak et al, 2001). Briefly, for each 30 min period, we perform two rotations to align the coordinate system with the flow streamlines, imposing zero lateral and vertical wind speed over the period. The planar fit method from Wilczak et al. (2001) was also tested, but it was unsuccessful due to

300   the presence of snow. In order to assess data quality, a random uncertainty quantification was used following Finkelstein and Sims (2001), which identified outliers, spikes, and artifacts. Finally, the 0-1-2 quality scheme from Mauder et al. (2013) was applied to flag the data, and segments that were flagged as 2 (poor quality) were removed from the data set.

To sort out the remaining outliers and to fill the gaps according to the EddyPro® procedure, post-processing was necessary. This was done using the PyFluxPro program (Isaac et al., 2017), which comprises six processing levels and uses EddyPro

305   output files as inputs and produces a continuous time series for all fluxes. For the first three processing levels, data were read, quality controlled, and finally, auxiliary measurements were merged when gaps were present. The quality control includes (i) range checks based on user-defined limits, (ii) spike detection, (iii) manual removal for specific dates, and (iv) data rejection based on other variables. Erroneous flux data were rejected based on CO_2 and H_2O signal strengths from the infrared gas analyzer (IRGA) and internal error codes from both the sonic anemometer and the IRGA. For the fourth processing level,

310   meteorological variables were gap-filled with ERA5 data. Each variable was bias-corrected using a linear fit between ERA5 and flux tower observations during periods when both were available.

Finally, the fluxes were gap-filled using interpolation and a self-organizing linear output map (SOLO) – a type of artificial neural network (ANN) (see Hsu et al. (2002) and Abramowitz (2005)). Interpolation was only applied for gaps of up to 3 hours, while SOLO was used for longer gaps. SOLO requires a set of environmental drivers such as air temperature, radiation, and

315   humidity, as well as the fluxes themselves as inputs. SOLO first constructs relationships between the environmental drivers by applying an ANN-equivalent of a principal component analysis. It then uses an ANN-equivalent of a multiple linear regression to make connections between the drivers and the fluxes. ANN together with marginal distribution sampling (MDS, Reichstein et al. (2005)) was shown to be the best choice for gap-filling flux data (Moffat et al., 2007). The resulting series for the sensible and latent heat fluxes, as well as the CO_2 fluxes, are shown in Fig. 8.

320   Since the IRGASON is an open-path sensor that is sensitive to external disturbances such as precipitation particles, gaps are frequently present in the data set for the turbulent and CO_2 fluxes. The fraction of gaps subsequently increased with each

processing step in EddyPro® and PyFluxPro. Overall, 27% of the sensible heat flux, 43% of the latent heat flux, and 44% of the CO_2 flux data were gap-filled using the SOLO. These values include two longer outages of IRGASON in March 2018 and from January to March 2019. The interpolated data and data gap-filled with SOLO are specifically flagged.
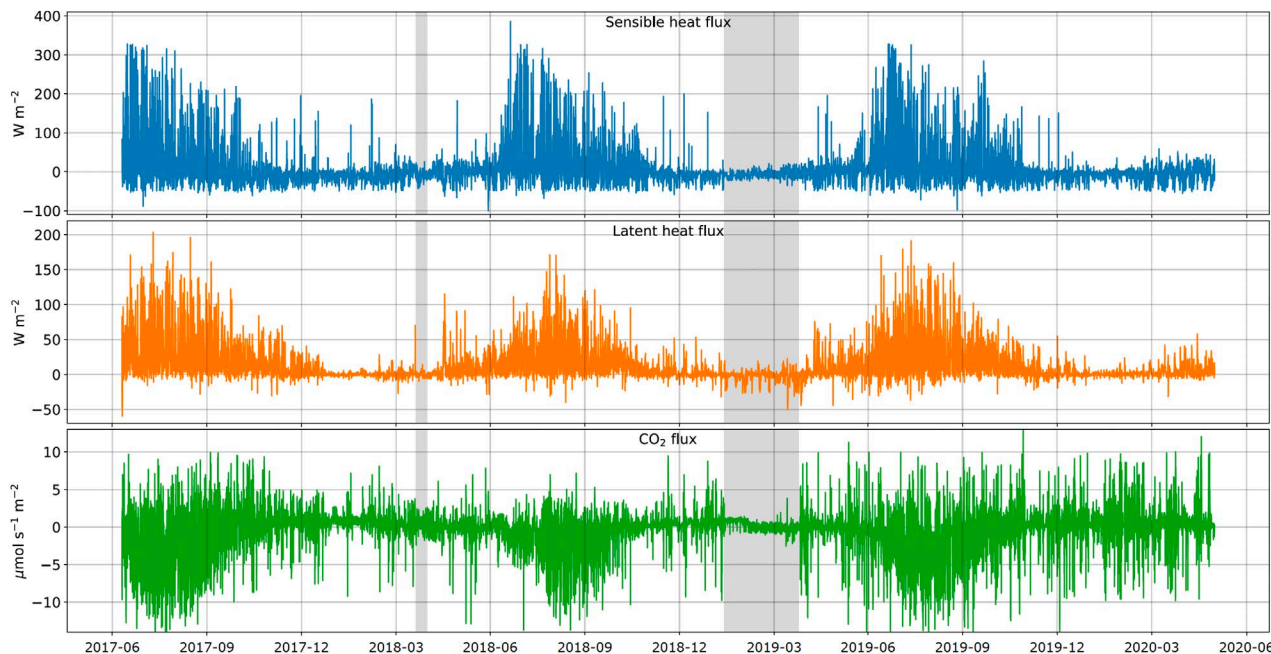
325

Figure 8: Time series of hourly sensible and latent heat fluxes and the CO_2 flux. The grey shaded areas indicate power outages at the station during which no flux data were recorded.

6 Snow Data

6.1 Snow Height

330   Two SR50 sonic distance sensors provided continuous snow height measurements near TUNDRA. One was installed exactly at the TUNDRA site and the other was mounted on the nearby 10-m tower. A snow height value of zero was assigned for the snow-free period in summer. Unfortunately, the snow height data were incomplete. We therefore decided to merge both data sets. The gaps that remained despite the merge were filled with estimates from time-lapse images of the snow poles. A similar SR50 sonic sensor was installed at FOREST. The sensor malfunctioned during winters 2016–17 and 2017–18 and no data are

335   shown for these periods. In spring, the snow height at FOREST almost reached the sensor. We observed during our field visits that the wind formed a depression on the snow surface just below the sensor. We thus estimate that snow height was underestimated by about 20% by the sensor in late March–early April. The time series for both stations are depicted in Fig. 9. Snow height values at FOREST are consistently larger than at TUNDRA due to the presence of taller vegetation, which more effectively traps blowing snow.
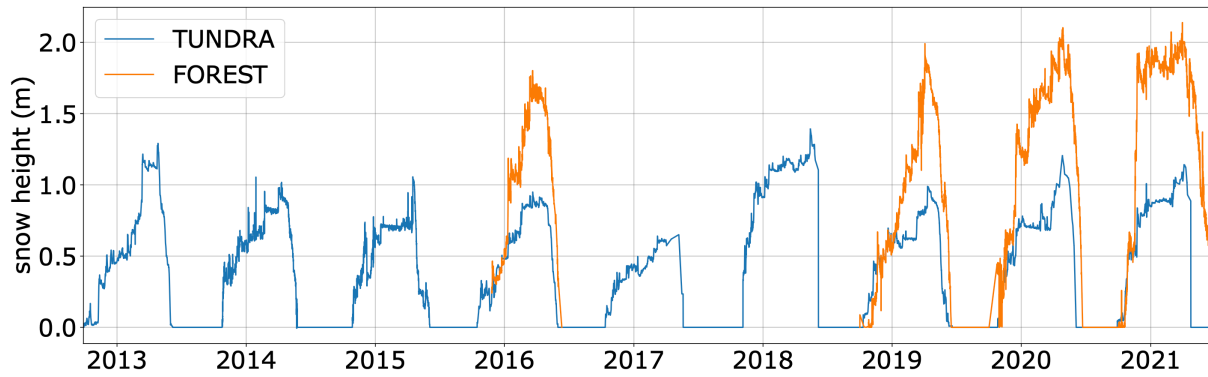
340

Figure 9: Evolution of snow height from the automatic gauges at TUNDRA and FOREST.

6.2 Snow Temperature

6.2.1 TUNDRA

345 Vertical profiles of snow temperature were recorded by two snow poles located approximately 4 m (SNOW1) and 15 m (SNOW2) from TUNDRA. They were equipped with Pt1000 thermistors (which are part of the TP08 needles) and collected temperature measurements every two days at 5:00 local summer time (UTC-4). SNOW1 was set up in February 2013 in a patch of shrubs about 30 cm tall with a lichen understory. The Pt1000 thermistors were installed at 4, 14, 34 and 44 cm above the lichen top surface. In September 2015, the post was replaced and the new pole was equipped with sensors at 4, 14, 29, 44 and

350 64 cm heights. SNOW2 was installed in 2018 on a patch of lichen. Four Pt1000 thermistors were placed at 7, 27, 47, and 67 cm above the lichen surface. SNOW1 data are shown in Fig. 10.

For both stations, data associated with a positive snow temperature were deleted as they implied that the sensor was not buried in the snow or that the sensor was heated by the sun through a thin snow layer. Using time-lapse images, we were able to identify times when the thermocouples/thermistors were not covered with snow. However, as the camera was 10 to 15 m away

355 from the stations, we cannot rule out that some data from times with no snow were included. Note that different snow heights and internal snow properties were observed at the two stations, and as such, the respective snow temperatures do not necessarily match for a similar measurement level.
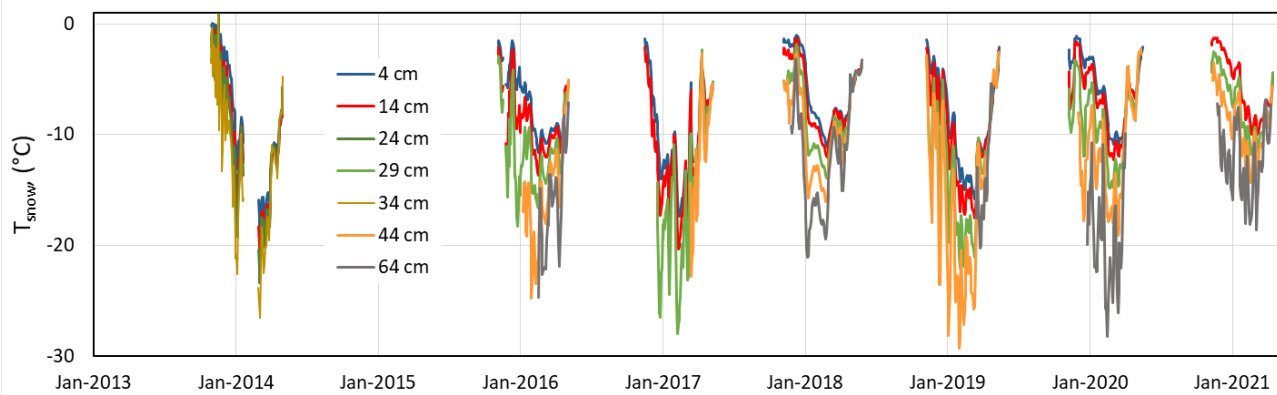
Figure 10: Bi-daily time series of the Pt1000 thermistors from the SNOW1 station at TUNDRA at heights of 4, 14, 24 and 34 cm for the 2013-2014 winter, and at heights of 4, 14, 29, 44 and 64 cm starting in October 2015.

6.2.3 FOREST

At FOREST, another snow pole (SNOW3) was installed and equipped with four Pt1000 thermistors at 4, 14, 29, and 64 cm heights. SNOW3 was placed in a patch of grass and moss. No time-lapse camera was available at FOREST, and as seen in Fig. 9, the snow height time series was less complete. Thus, only fall positive temperatures were removed and no further data cleaning was performed. In spring, the first positive temperatures were left, as they provide an indication of snow melt down to the level of the sensor. Figure 11 shows the snow temperature at the four measurement levels. Snow temperatures were substantially higher at FOREST due to the deeper snowpack.
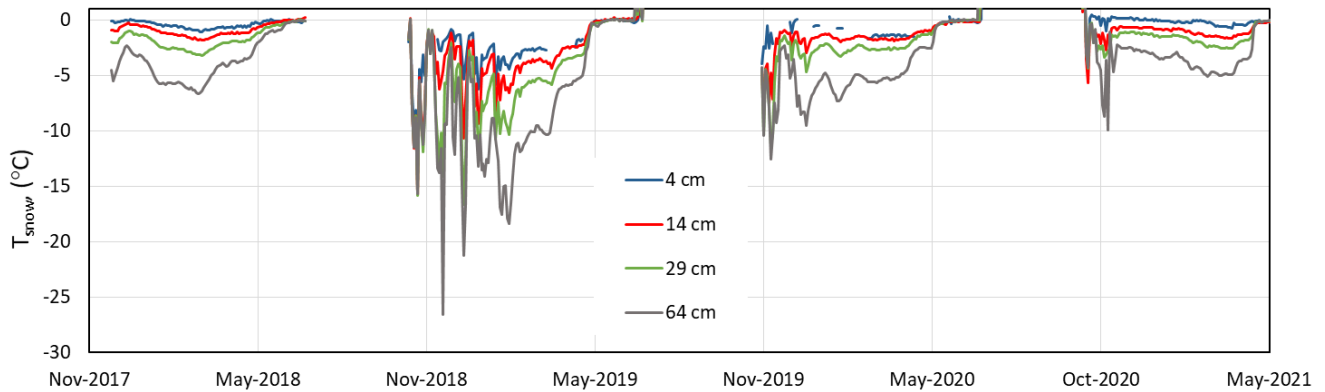
Figure 11: Hourly time series of the Pt1000 thermistors from the SNOW3 station at heights of 4, 14, 29, and 64 cm.

6.3 Snow Thermal Conductivity

6.3.1 TUNDRA

TP08 heated needle probes were installed along with the temperature probes at both SNOW1 and SNOW2. The installation heights were the same as those for the Pt1000 thermistors. A description of the method used to determine the snow effective thermal conductivity from the TP08 heated needle probes is provided in Domine et al. (2015). It is reminded that since the TP08 heat the snow, the measurement is deactivated by a temperature threshold (–2.5°C) so that there are data gaps. Figure 12 shows the observations from SNOW1 at five heights over 9 winters.
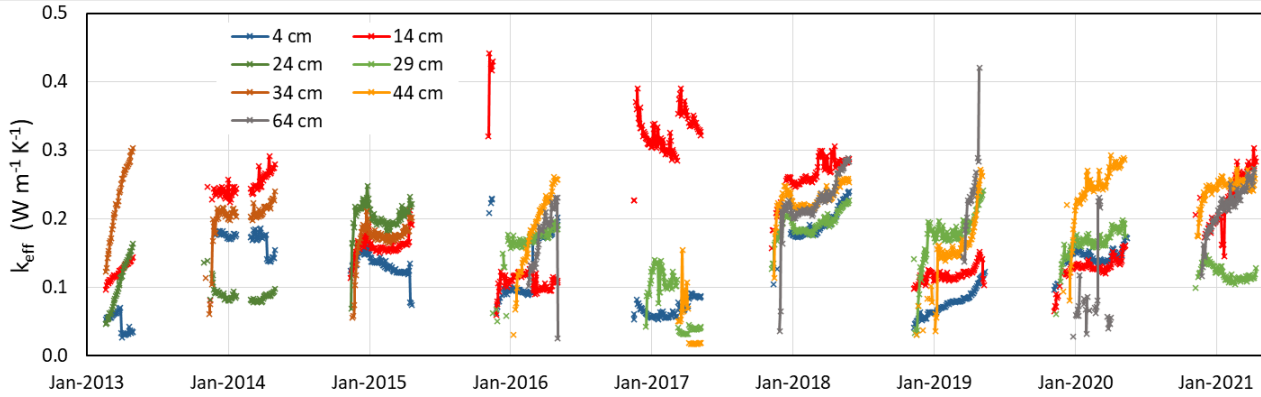
Figure 12: Time series of the snow thermal conductivity from the SNOW1 station at heights of 4, 14, 24 and 34 cm from February 2013 to May 2015 and at heights of 4, 14, 29, 44 and 64 cm starting in October 2015.

6.3.2 FOREST

The thermal conductivity at FOREST was also recorded with the TP08 heated needles at SNOW3. These were also installed at the same heights as the Pt1000 temperature sensors. Since the sensor at 14 cm did not work properly, the corresponding values were not included. Because of the temperature threshold, the 4 cm sensor recorded data only during the 2018-2019 winter, and also a few data points during the following winter. The recorded values are shown in Fig. 13.
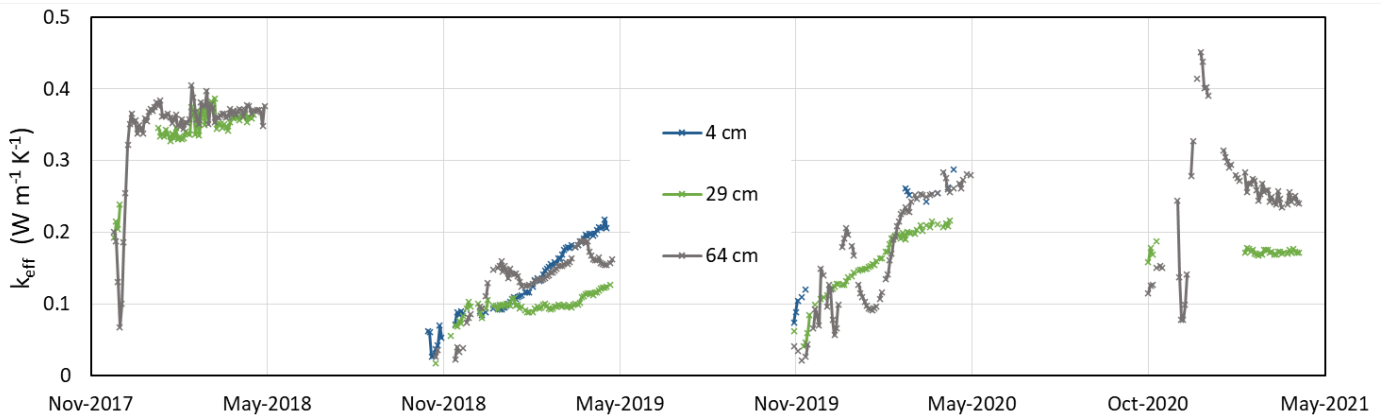
Figure 13: Time series of the snow thermal conductivity from the SNOW3 station at heights of 4, 29 and 64 cm.

6.4 Snow Pit Measurements

Field trips were conducted most years to measure vertical profiles of snow density and snow specific surface area (SSA). Snow density was measured with a 100 cm^3 box cutter (Conger and McClung, 2009) and a field scale, while SSA was measured using infrared reflectance at 1310 nm with an integrating sphere as described in Gallet et al. (2009). One to three field trips were made each year, between late January and early April. The last field trip was in 2019, since travel in 2020 and 2021 was forbidden because of the COVID pandemic. The available snow data therefore provide an overview of the snow properties in mid-winter and early spring. In most pits, snow density and SSA were measured in sequence. However, in some pits, only density was measured. It was often not possible to measure density near the base of the snowpack, because of the dense birch branches. The snow there was usually soft depth hoar, which could be scooped into the SSA sampler without alteration to SSA, so that SSA profiles often go down to the snow base. Ice layers or layers with melt forms were observed in the majority of snow pits and were sometimes impossible to sample because they were too hard. The profiles of snow density and SSA near the TUNDRA and the FOREST sites are illustrated in Fig. 14. Note that the representativity of the measured profiles is limited, as the physical snow properties are highly spatially variable due to vegetation, micro-topography, and wind erosion and redeposition. However, at TUNDRA, the general trend of slight density increase with increasing height, except for recent snowfalls near the top, is consistent and typical of the Arctic (Domine et al., 2016). Figure 14 illustrates that the SSA of the basal depth hoar is always close to 10 m^2 kg^{-1} (Royer et al., 2021).
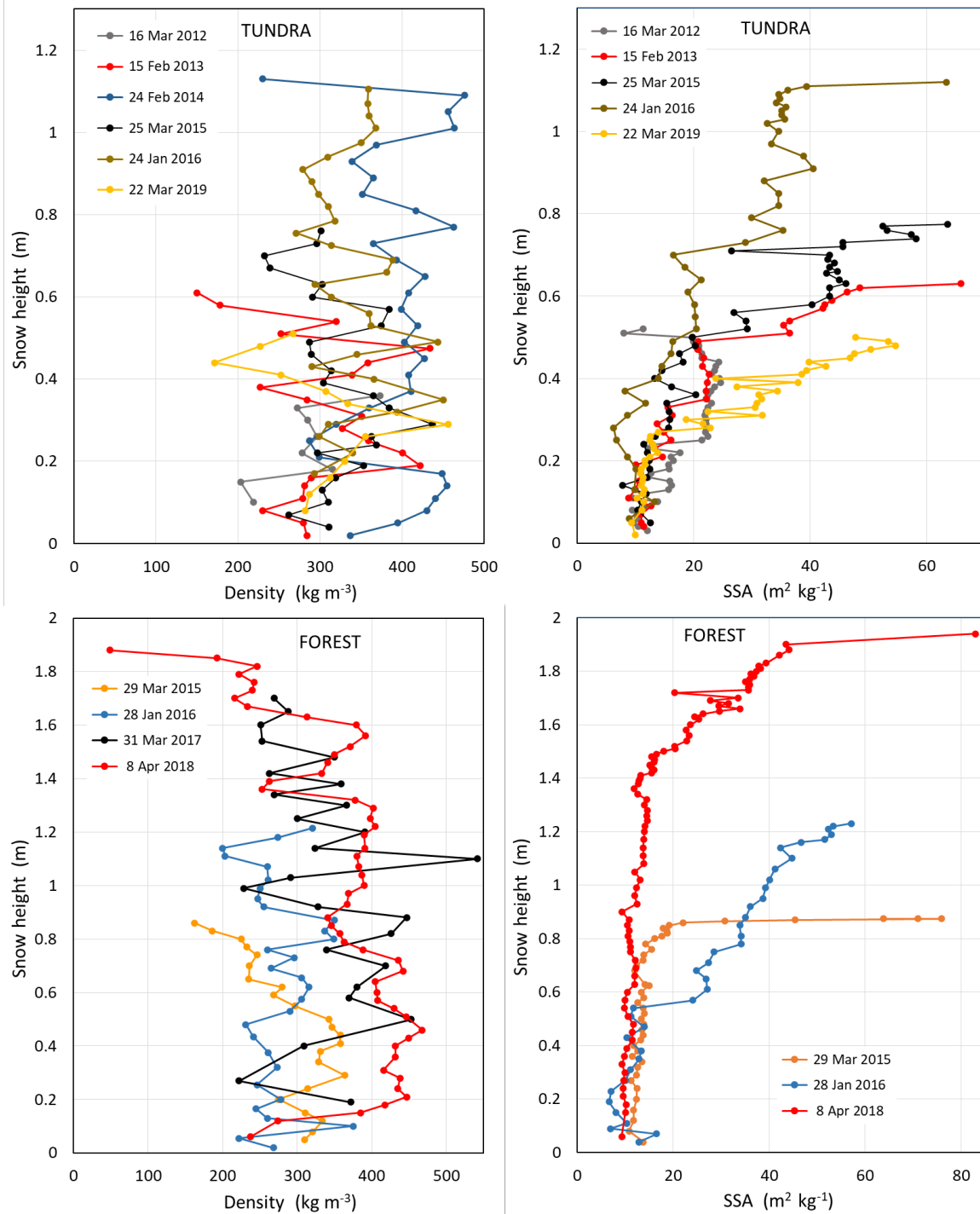
Figure 14: Vertical profiles of snow density and SSA measured in the vicinity of the TUNDRA station from 2012 to 2019 and near the FOREST station from 2016 to 2018.

7. Soil Data

7.1 Soil Properties

The Tasiapik Valley consists of former beaches that have been uplifted by isostatic rebound after the Laurentide Ice Sheet melted a few millennia ago. According to Bhiry et al. (2011), land at an elevation of around 130 m, such as the TUNDRA site, emerged 6500 to 7000 years ago. The FOREST site, at an elevation 82 m, emerged about 5000 years ago. Because they were formerly beaches, the soil at both TUNDRA and FOREST sites is mostly sandy. Gagnon et al. (2019) conducted granulometric analyses at TUNDRA and reported a unimodal particle size distribution of around 500 μm (pure sand), with an occasional, small, secondary peak at around 80 μm (loamy sand). Based on two soil pits, we estimate the sand fraction of the soil at FOREST to be lower than at TUNDRA, but no granulometric analyses were performed there.

The organic carbon content of the soil at TUNDRA is among the lowest in the Arctic and subarctic (Gagnon et al., 2019), with about 1.5 kg m^{-2} of organic C in lichen tundra, and 4.2 kg m^{-2} in low birch shrubs (< 80 cm). No detailed soil analyses were performed at FOREST, but two soil pits were dug and revealed an organic litter layer 6 to 10 cm thick. The organic carbon content of the soil at FOREST was not measured, but given the thick litter layer, it is probably greater than at TUNDRA.

Soil thermal conductivity and density profiles are shown in Fig. 15. On 7 and 8 October 2014, short-distance spatial variation tests were performed at a depth of 20 cm, revealing changes within a range of 25% over a horizontal distance of 30 cm. Overall, there was a clear trend for an increase in thermal conductivity with depth. The thermal conductivity of lichen was also measured and it was essentially the same as that of air, forming an efficient insulating layer in summer. In winter, snow crystals blend into the lichen. Therefore, we determined that assuming only a depth hoar snow layer while ignoring the lichen is likely adequate. We recommend using thermal conductivities of 0.12 W m^{-1} K^{-1} for the top 5 cm of the soil (starting at the base of the live lichen), 0.5 W m^{-1} K^{-1} for depths between 5 and 10 cm, 0.9 W m^{-1} K^{-1} between 10 and 20 cm, and 1.1 W m^{-1} K^{-1} for depths below 20 cm. We only measured three density profiles, which showed an increase in density down to 10 cm in depth, and then remained at an almost constant value of around 1500 kg m^{-3}. Between depths of 0 and 10 cm, the density is about 500 kg m^{-3} for the litter layer and approximately 1000 kg m^{-3} For the underlying mineral layer. Sand has a specific heat of about 796 J kg^{-1} K^{-1} (Carvill, 1993).
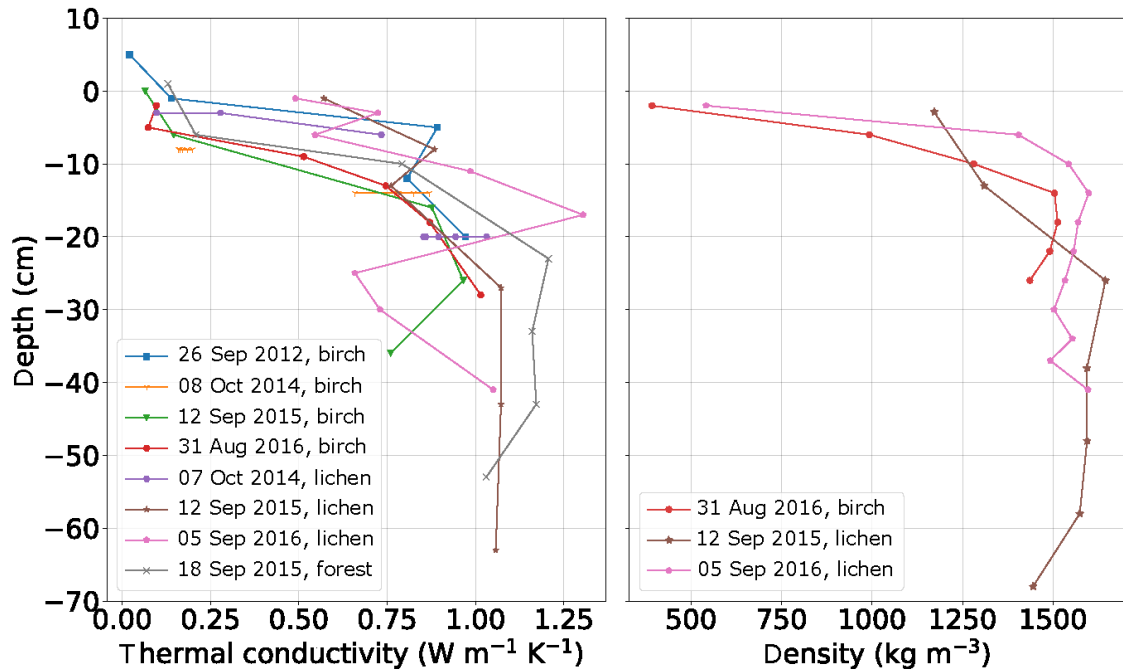
Figure 15: Thermal properties of soils. (a) Thermal conductivity; (b) density. Depths were measured from the base of the live lichen.

7.2 Soil Temperature and Moisture

440 Soil temperatures at TUNDRA and FOREST were recorded using 5TM soil temperature and water content sensors. According to 5TM specifications, the resolution is 0.1°C for the soil temperature and 0.0008 m^3 m^{-3} for the soil water content. The accuracy is 1°C for the temperature and 0.03 m^3 m^{-3} for the soil water content. At all the stations, we observed offsets during the zero-curtain period, when $T = 0$°C. The temperatures were corrected for these offsets, ranging between 0.2°C and 0.6°C.

7.2.1 TUNDRA

445 The soil temperature and soil water content were measured at two lichen sites near TUNDRA. One of these sites also had 30 cm tall birch shrubs, and was about 1 m from the SNOW1 post. Five Decagon 5TM probes were installed at each site. Figure 6 shows these values for a lichen-only-covered surface, while Fig. 7 shows values for the site with low birch shrubs. The soil temperature at the lichen site is warmer during the summer months compared to the low-shrub site, and the soil water content is generally lower. This might be due to shading from the shrubs and the differences in soil composition, as detailed in Sect. 450 7.2.
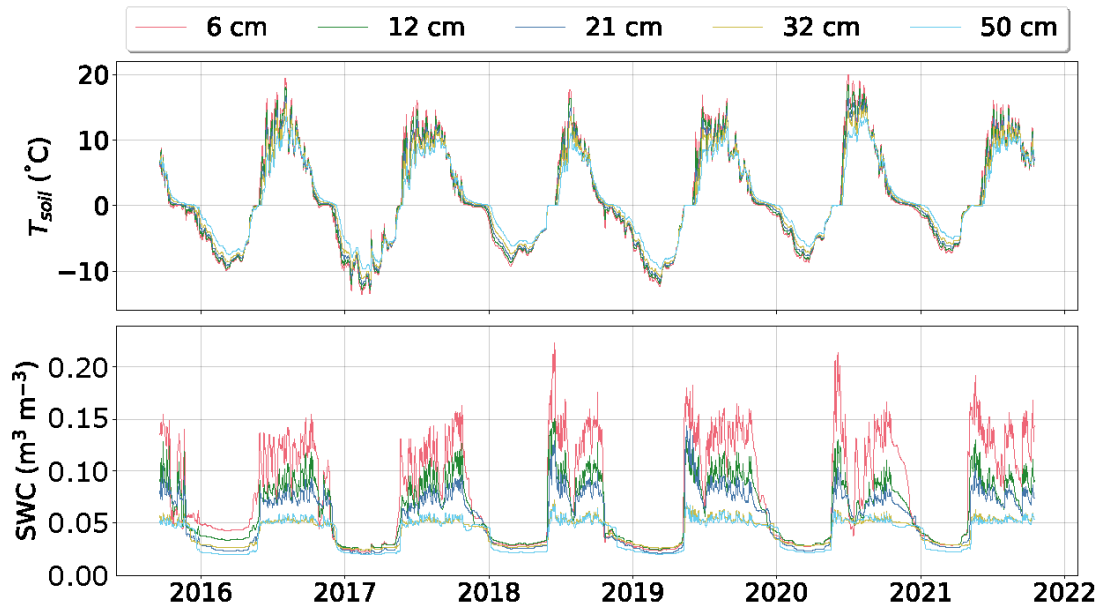
Figure 16: Time series of the daily soil temperature and the soil water content (SWC) under a lichen-covered surface at depths of 6 cm, 12 cm, 21 cm, 39 cm, and 50 cm at TUNDRA.

455
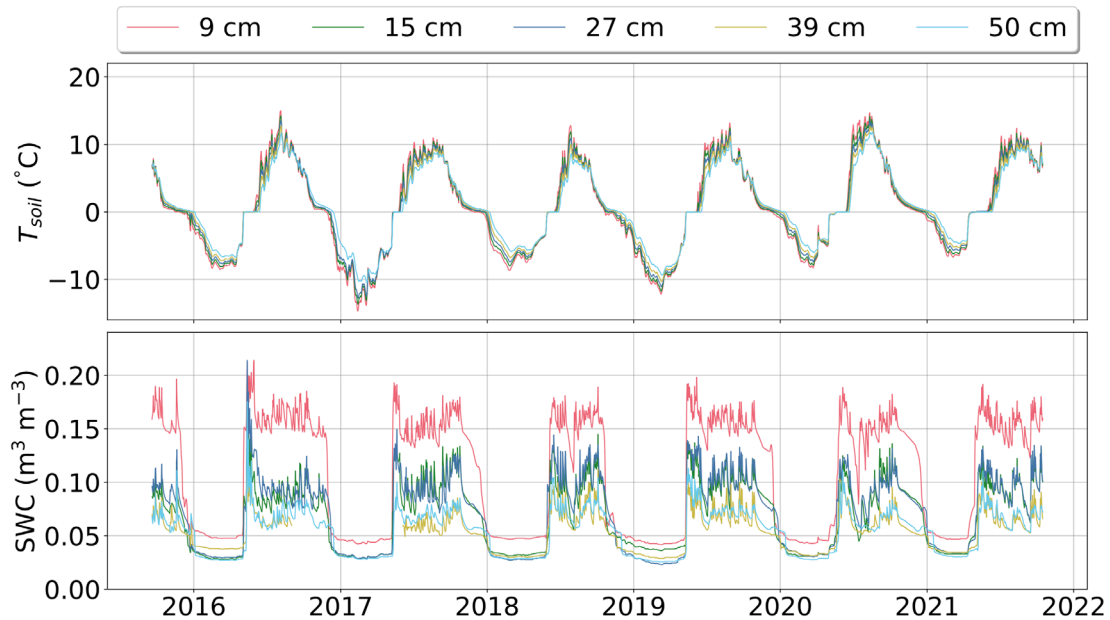
Figure 17: Time series of the daily soil temperature and the soil volume water content (SWC) under a patch of low shrubs over lichen at depths of 9 cm, 15 cm, 27 cm, 39 cm, and 50 cm at TUNDRA.

7.2.2 FOREST

The soil temperature and water content were measured at FOREST using the same instruments as the TUNDRA site (Fig. 18).

460   The sensors were placed about 80 cm from the SNOW3 pole. The soil water content and temperatures at FOREST were very distinct from those measured at the TUNDRA site. During summer, the soil temperatures were slightly cooler than those under the low-shrub surface. However, in winter, the soil freezes late and the minimum temperatures were only slightly below 0°C due to the thick snow cover. The soil water content is substantially higher at FOREST than at TUNDRA because the soil contains less sand compared to TUNDRA and because more snow accumulates in winter at FOREST and melts in spring.

465
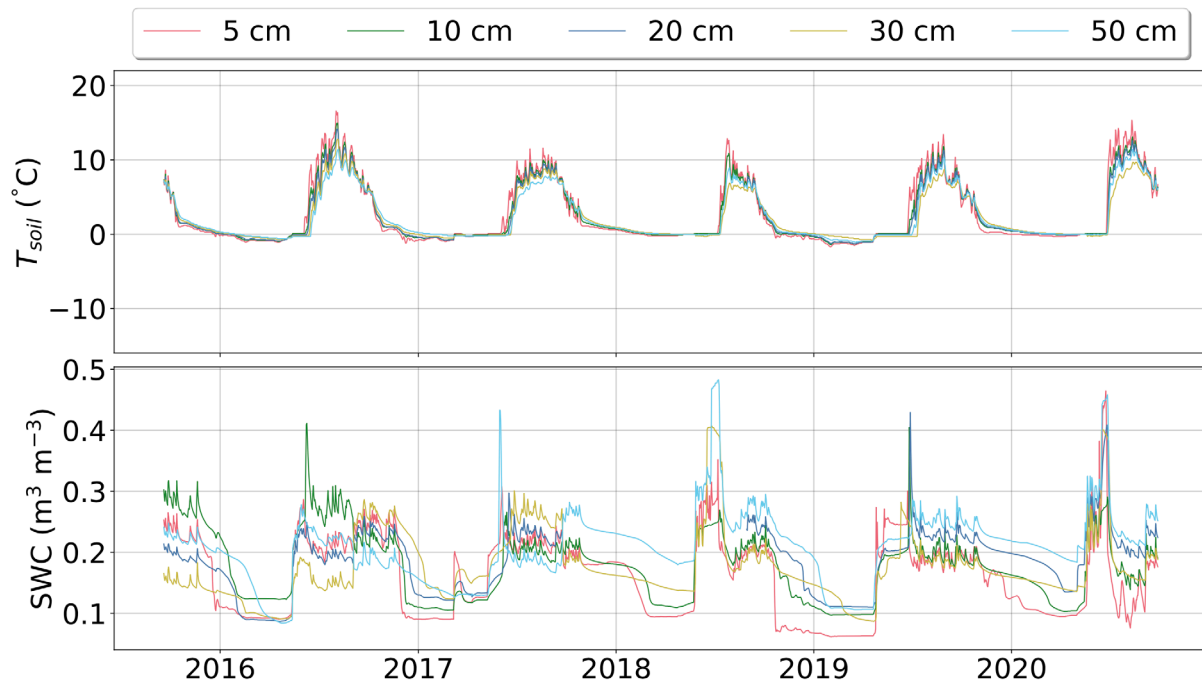
Figure 18: Time series of the daily soil temperature and the soil volume water content (SWC) below grass and moss at depths of 5 cm, 10 cm, 20 cm, 30 cm and 50 cm at FOREST.

8. Conclusions

The increasing temperatures in Arctic regions are causing substantial environmental changes, such as the thawing of permafrost

470   and the greening of the Arctic landscapes. Both effects are more pronounced along the southern border of the Arctic, where the land is transitioning into a boreal forest. In this study, we present two data sets, a 9-year data set for TUNDRA and a 6-year data set for FOREST which include numerous measurements in soil, snow and above the ground at two sites along the treeline in eastern Canada. These data provide information that can be used to calibrate and improve earth system models, particularly snow and land surface schemes, which have previously shown poor performance when simulating Arctic snowpack

475   properties (Domine et al., 2019). Our data can help advance the understanding of the relationships between potential meteorological drivers, permafrost degradation and Arctic greening.

Acknowledgements.

This work was funded by the French Polar Institute (IPEV), the Natural Sciences and Engineering Research Council of Canada (Discovery Grant and Northern Research supplement programs), the BNP-Paribas foundation (APT project), and the European Union's Horizon 2020 research and innovation program under grant agreement No. 101003536 (ESM2025 – Earth System Models for the Future) and grant agreement No. 727890 (INTAROS). We thank the community of Umiujaq for welcoming us and allowing this research to be conducted. We benefited from facilities from the Centre d'Études Nordiques during the entire duration of this study. Compute Canada assisted with data storage and handling. This work is a contribution to the IASC project Terrestrial Multidisciplinary distributed Observatories for the Study of Arctic Connections (T-MOSAiC).

480

Data availability

485

The data are available on the PANGAEA repository, https://doi.org/10.1594/PANGAEA.XXXXXX (Domine et al., 2024), as tab-delimited text files. All times are UTC.

Author contributions.

FD, GL and DN designed the research. FD and DN obtained funding. DS, FD, GL, and DN deployed and maintained the instruments. FD and GL analyzed the data and prepared the data files. FD, GL, and MBB performed the fieldwork. GL and FD wrote the paper with comments from MBB, DS and DN.

490

Competing interests

The authors declare that they have no conflict of interest.

495

References

Abramowitz, G.: Towards a benchmark for land surface models, Geophysical Research Letters, 32, L22 702, https://doi.org/10.1029/2005GL024419, 2005.

Barrere, M., Domine, F., Decharme, B., Morin, S., Vionnet, V., and Lafaysse, M.: Evaluating the performance of coupled snow–soil mod- els in SURFEXv8 to simulate the permafrost thermal regime at a high Arctic site, Geoscientific Model Development, 10, 3461–3479, https://doi.org/10.5194/gmd-10-3461-2017, 2017.

Bhiry, N., Delwaide, A., Allard, M., Bégin, Y., Filion, L., Lavoie, M., Nozais, C., Payette, S., Pienitz, R., Émilie Saulnier-Talbot, and Vincent, W. F.: Environmental change in the Great Whale River region, Hudson Bay: Five decades of multidisciplinary research by Centre d'études nordiques (CEN), Écoscience, 18, 182–203, https://doi.org/10.2980/18-3-3469, 2011.

Boisvert, L. N., Wu, D. L., Vihma, T., and Susskind, J.: Verification of air/surface humidity differences from AIRS and ERA- Interim in support of turbulent flux estimation in the Arctic, Journal of Geophysical Research: Atmospheres, 120, 945–963, https://doi.org/https://doi.org/10.1002/2014JD021666, 2015.

Callaghan, T. V., Crawford, R. M. M., Eronen, M., Hofgaard, A., Payette, S., Rees, W. G., Skre, O., Sveinbjörnsson, B., Vlassova, T. K., and Werkman, B. R.: The dynamics of the Tundra-Taiga Boundary: An overview and suggested coordinated and integrated approach to research, Ambio, pp. 12:3–5, http://www.jstor.org/stable/25094569, 2002.

Carvill, J.: 3 - Thermodynamics and heat transfer, in: Mechanical Engineer's Data Handbook, edited by Carvill, J., pp. 102–145, Butterworth- Heinemann, Oxford, https://doi.org/10.1016/B978-0-08-051135-1.50008-X, 1993.

CEN: Climate station data from the Umiujaq region in Nunavik, Quebec, Canada, https://doi.org/10.5885/45120SL-067305A53E914AF0, accessed: 2022-06-20, 1997-2020.

Conger, S. and McClung, D.: Instruments and methods comparison of density cutters for snow profile observations, Journal of Glaciology, 55, 163–169, https://doi.org/10.3189/002214309788609038, 2009.

Domine, F., Barrere, M., Sarrazin, D., Morin, S., and Arnaud, L.: Automatic monitoring of the effective thermal conductivity of snow in a low-Arctic shrub tundra, The Cryosphere, 9, 1265–1276, https://doi.org/10.5194/tc-9-1265-2015, 2015.

Domine, F., Picard, G., Morin, S., Barrere, M., Madore, J.-B., and Langlois, A.: Major Issues in Simulating Some Arctic Snowpack Properties Using Current Detailed Snow Physics Models: Consequences for the Thermal Regime and Water Budget of Permafrost, Journal of Advances in Modeling Earth Systems, 11, 34-44, https://doi.org/10.1029/2018MS001445, 2019.

Domine, F., Barrere, M., and Sarrazin, D.: Seasonal evolution of the effective thermal conductivity of the snow and the soil in high Arctic herb tundra at Bylot Island, Canada, The Cryosphere, 10, 2573–2588, https://doi.org/10.5194/tc-10-2573-2016, 2016.

Domine, F., Lackner, G., Sarrazin, D., Poirier, M., and Belke-Brea, M.: Meteorological, snow and soil data (2013–2019) from a herb tundra permafrost site at Bylot Island, Canadian high Arctic, for driving and testing snow and land surface models, Earth Syst. Sci. Data, 13, 4331-4348, https://doi.org/10.5194/essd-13-4331-2021, 2021.

Domine, F., Sarrazin, D., Nadeau, D., Lackner, G. and Belke-Brea, M.: Hydrometeorological, snow and soil data from a low-Arctic valley in the forest-tundra ecotone in Northern Quebec. PANGAEA, https://doi.org/10.1594/PANGAEA.XXXXXX, 2024.

Finkelstein, P. L. and Sims, P. F.: Sampling error in eddy correlation flux measurements, Journal of Geophysical Research: Atmospheres, 106, 3503–3509, https://doi.org/10.1029/2000JD900731, 2001.

Gagnon, M., Domine, F., and Boudreau, S.: The carbon sink due to shrub growth on Arctic tundra: a case study in a carbon-poor soil in eastern Canada, Environmental Research Communications, 1, 091001, https://doi.org/10.1088/2515-7620/ab3cdd, 2019.

Gallet, J.-C., Domine, F., Zender, C. S., and Picard, G.: Measurement of the specific surface area of snow using infrared reflectance in an integrating sphere at 1310 and 1550 nm, The Cryosphere, 3, 167–182, https://doi.org/10.5194/tc-3-167-2009, 2009.

Gouttevin, I., Langer, M., Löwe, H., Boike, J., Proksch, M., and Schneebeli, M.: Observation and modelling of snow at a polygonal tundra permafrost site: spatial variability and thermal implications, The Cryosphere, 12, 3693–3717, https://doi.org/10.5194/tc-12-3693-2018, 2018.

Guo, W., Rees, G., and Hofgaard, A.: Delineation of the forest-tundra ecotone using texture-based classification of satellite imagery, Inter- national Journal of Remote Sensing, 41, 6384–6408, https://doi.org/10.1080/01431161.2020.1734254, 2020.Hsu, K.-l., Gupta, H. V., Gao, X., Sorooshian, S., and Imam, B.: Self-organizing linear output map (SOLO): An artificial neural network suitable for hydrologic modeling and analysis, Water Resources Research, 38, 38–1–38–17, https://doi.org/10.1029/2001WR000795, 2002.

Hersbach, H., Bell, B., Berrisford, P., Hirahara, S., Horányi, A., Muñoz-Sabater, J., Nicolas, J., Peubey, C., Radu, R., Schepers, D., Simmons, A., Soci, C., Abdalla, S., Abellan, X., Balsamo, G., Bechtold, P., Biavati, G., Bidlot, J., Bonavita, M., De Chiara, G., Dahlgren, P., Dee, D., Diamantakis, M., Dragani, R., Flemming, J., Forbes, R., Fuentes, M., Geer, A., Haimberger, L., Healy, S., Hogan, R. J., Hólm, E., Janisková, M., Keeley, S., Laloyaux, P., Lopez, P., Lupu, C., Radnoti, G., de Rosnay, P., Rozum, I., Vamborg, F., Villaume, S., and Thépaut, J.-N.: The ERA5 global reanalysis, Q. J. Roy. Meteorol. Soc., 146, 1999-2049, https://doi.org/10.1002/qj.3803, 2020.

Isaac, P., Cleverly, J., McHugh, I., van Gorsel, E., Ewenz, C., and Beringer, J.: OzFlux data: network integration from collection to curation, Biogeosciences, 14, 2903–2928, https://doi.org/10.5194/bg-14-2903-2017, 2017.

Jafari, M., Gouttevin, I., Couttet, M., Wever, N., Michel, A., Sharma, V., Rossmann, L., Maass, N., Nicolaus, M., and Lehning, M.: The impact of diffusive water vapor transport on snow profiles in deep and shallow snow covers and on sea ice, Frontiers in Earth Science, 8, 249, https://doi.org/10.3389/feart.2020.00249, 2020.

Jiménez, C., Michel, D., Hirschi, M., Ermida, S., and Prigent, C.: Applying multiple land surface temperature prod- ucts to derive heat fluxes over a grassland site, Remote Sensing Applications: Society and Environment, 6, 15–24, https://doi.org/https://doi.org/10.1016/j.rsase.2017.01.002, 2017.

Jones, B.: Recent Arctic tundra fire initiates widespread thermokarst development, Scientific Reports, 5, 15 865, https://doi.org/10.1038/srep15865, 2015.

Kochendorfer, J., Nitu, R., Wolff, M., Mekis, E., Rasmussen, R., Baker, B., Earle, M. E., Reverdin, A., Wong, K., Smith, C. D., Yang, D., Roulet, Y.-A., Meyers, T., Buisan, S., Isaksen, K., Brækkan, R., Landolt, S., and Jachcik, A.: Testing and development of transfer functions for weighing precipitation gauges in WMO-SPICE, Hydrol. Earth Syst. Sci., 22, 1437–1452, https://doi.org/10.5194/hess-22-1437-2018, 2018.

Krinner, G., Derksen, C., Essery, R., Flanner, M., Hagemann, S., Clark, M., Hall, A., Rott, H., Brutel-Vuilmet, C., Kim, H., Ménard, C. B., Mudryk, L., Thackeray, C., Wang, L., Arduini, G., Balsamo, G., Bartlett, P., Boike, J., Boone, A., Chéruy, F., Colin, J., Cuntz, M., Dai, Y., Decharme, B., Derry, J., Ducharne, A., Dutra, E., Fang, X., Fierz, C., Ghattas, J., Gusev, Y., Haverd, V., Kontu, A., Lafaysse, M., Law, R., Lawrence, D., Li, W., Marke, T., Marks, D., Ménégoz, M., Nasonova, O., Nitta, T., Niwano, M., Pomeroy, J., Raleigh, M. S., Schaedler, G., Semenov, V., Smirnova, T. G., Stacke, T., Strasser, U., Svenson, S., Turkov, D., Wang, T., Wever, N., Yuan, H., Zhou, W., and Zhu, D.: ESM-SnowMIP: assessing snow models and quantifying snow-related climate feedbacks, Geoscientific Model Development, 11, 5027–5049, https://doi.org/10.5194/gmd-11-5027-2018, 2018.

Lackner, G., Domine, F., Sarrazin, D., Nadeau, D., and Belke-Brea, M.: Hydrometeorological, snow and soil data from a low-Arctic valley in the forest-tundra ecotone in Northern Quebec. PANGAEA, https://doi.org/10.1594/PANGAEA.946538, 2022b.

Latifovic, R., Pouliot, D., and Olthof, I.: Circa 2010 Land Cover of Canada: Local Optimization Methodology and Product

Development, Remote Sensing, 9, https://doi.org/10.3390/rs9111098, 2017.

Lemieux, J.-M., Fortier, R., Murray, R., Dagenais, S., Cochand, M., Delottier, H., Therrien, R., Molson, J., Pryet, A., and Parhizkar, M.: Groundwater dynamics within a watershed in the discontinuous permafrost zone near Umiujaq (Nunavik, Canada), Hydrogeology Journal, 28, https://doi.org/10.1007/s10040-020-02110-4, 2020.

Mack, M., Bret-Harte, M., Hollingsworth, T., Jandt, R., Schuur, E., Shaver, G., and Verbyla, D.: Carbon loss from an unprecedented Arctic tundra wildfire, Nature, 475, 489–92, https://doi.org/10.1038/nature10283, 2011.

Martin, M. A., Ghent, D., Pires, A. C., Göttsche, F.-M., Cermak, J., and Remedios, J. J.: Comprehensive in situ validation of five satellite land surface temperature data sets over multiple stations and years, Remote Sensing, 11, https://doi.org/10.3390/rs11050479, 2019.

Mauder, M., Cuntz, M., Drüe, C., Graf, A., Rebmann, C., Schmid, H. P., Schmidt, M., and Steinbrecher, R.: A strategy for qual- ity and uncertainty assessment of long-term eddy-covariance measurements, Agricultural and Forest Meteorology, 169, 122 – 135, https://doi.org/10.1016/j.agrformet.2012.09.006, 2013.

Meredith, M., Sommerkorn, M., Cassotta, S., Derksen, C., Ekaykin, A., Hollowed, A., Kofinas, G., Mackintosh, A., Melbourne-Thomas, J., Muelbert, M., Ottersen, G., Pritchard, H., and Schuur, E.: Polar Regions. In:IPCC Special Report on the Ocean and Cryosphere in a Changing Climate [H.-O. Pörtner, D.C. Roberts, V.Masson-Delmotte, P. Zhai, M. Tignor, E. Poloczanska, K. Mintenbeck, A. Alegria, M. Nicolai, A. Okem, J. Petzold, B. Rama, N.M. Weyer (eds.), https://www.ipcc.ch/srocc/, 2019.

Moffat, A. M., Papale, D., Reichstein, M., Hollinger, D. Y., Richardson, A. D., Barr, A. G., Beckstein, C., Braswell, B. H., Churkina, G., Desai, A. R., Falge, E., Gove, J. H., Heimann, M., Hui, D., Jarvis, A. J., Kattge, J., Noormets, A., and Stauch, V. J.: Comprehen- sive comparison of gap-filling techniques for eddy covariance net carbon fluxes, Agricultural and Forest Meteorology, 147, 209 – 232, https://doi.org/10.1016/j.agrformet.2007.08.011, 2007.

Moncrieff, J., Massheder, J., de Bruin, H., Elbers, J., Friborg, T., Heusinkveld, B., Kabat, P., Scott, S., Soegaard, H., and Verhoef, A.: A system to measure surface fluxes of momentum, sensible heat, water vapour and carbon dioxide, Journal of Hydrometeorology, 188-189, 589 – 611, https://doi.org/https://doi.org/10.1016/S0022-1694(96)03194-0, hAPEX-Sahel, 1997.

Pearson, R., Phillips, S., Loranty, M., Beck, P., Damoulas, T., Knight, S., and Goetz, S.: Shifts in Arctic vegetation and associated feedbacks under climate change, Nature Climate Change, 3, 673–677, https://doi.org/10.1038/nclimate1858, 2013.

Pedregosa, F., Varoquaux, G., Gramfort, A., Michel, V., Thirion, B., Grisel, O., Blondel, M., Prettenhofer, P., Weiss, R., Dubourg, V., Vanderplas, J., Passos, A., Cournapeau, D., Brucher, M., Perrot, M., and Duchesnay, E.: Scikit-learn: Machine Learning in Python, Journal of Machine Learning Research, 12, 2825–2830, 2011.

Qu, M., Pang, X., Zhao, X., Zhang, J., Ji, Q., and Fan, P.: Estimation of turbulent heat flux over leads using satellite thermal images, The Cryosphere, 13, 1565–1582, https://doi.org/10.5194/tc-13-1565-2019, 2019.

Reichstein, M., Falge, E., Baldocchi, D., Papale, D., Aubinet, M., Berbigier, P., Bernhofer, C., Buchmann, N., Gilmanov, T., Granier, A., Grünwald, T., Havránková, K., Ilvesniemi, H., Janous, D., Knohl, A., Laurila, T., Lohila, A., Loustau, D., Matteucci, G., Meyers, T., Miglietta, F., Ourcival, J.-M., Pumpanen, J., Rambal, S., Rotenberg, E., Sanz, M., Tenhunen, J., Seufert, G., Vaccari, F., Vesala, T., Yakir, D., and Valentini, R.: On the separation of net ecosystem exchange into assimilation and ecosystem respiration: Review and improved algorithm, Global Change Biology, 11, 1424–1439, https://doi.org/10.1111/j.1365-2486.2005.001002.x, 2005.

Riihelä, A., Key, J. R., Meirink, J. F., Kuipers Munneke, P., Palo, T., and Karlsson, K.-G.: An intercomparison and validation of satellite-based surface radiative energy flux estimates over the Arctic, Journal of Geophysical Research: Atmospheres, 122, 4829–4848, https://doi.org/https://doi.org/10.1002/2016JD026443, 2017.

Robichaud, B. and Mullock, J.: The Weather of Atlantic Canada and Eastern Quebec, NAV Canada, 2001.

625   Royer, A., Domine, F., Roy, A., Langlois, A., Marchand, N., and Davesne, G.: New northern snowpack classification linked to vegetation cover on a latitudinal mega-transect across northeastern Canada, Écoscience, 28, 225–242, https://doi.org/10.1080/11956860.2021.1898775, 2021.

Simson, A., Löwe, H., and Kowalski, J.: Elements of future snowpack modeling – Part 2: A modular and extendable Eulerian–Lagrangian numerical scheme for coupled transport, phase changes and settling processes, The Cryosphere, 15, 5423–
630   5445, https://doi.org/10.5194/tc- 15-5423-2021, 2021.

Webb, E. K., Pearman, G. I., and Leuning, R.: Correction of flux measurements for density effects due to heat and water vapour transfer, Quart. J. Roy. Meteor. Soc., 106, 85–100, https://doi.org/10.1002/qj.49710644707, 1980.

Wilczak, J., Oncley, S., and Stage, S.: Sonic anemometer tilt correction algorithms, Boundary-Layer Meteorology, 99, https://doi.org/10.1023/A:1018966204465, 2001.

635